

pubs.acs.org/acssensors Article

Texaphyrin-Based Calcium Sensor for Multimodal Imaging

Grégory D. Thiabaud, Miriam Schwalm, Sajal Sen, Ali Barandov, Jacob Simon, Peter Harvey, Virginia Spanoudaki, Peter Müller, Jonathan L. Sessler, and Alan Jasanoff*



Cite This: ACS Sens. 2023, 8, 3855-3861



ACCESS I

Metrics & More

Article Recommendations

s Supporting Information

ABSTRACT: The ability to monitor intracellular calcium concentrations using fluorescent probes has led to important insights into biological signaling processes at the cellular level. An important challenge is to relate such measurements to broader patterns of signaling across fields of view that are inaccessible to optical techniques. To meet this need, we synthesized molecular probes that couple calcium-binding moieties to lanthanide texaphyrins, resulting in complexes endowed with a diverse complement of magnetic and photophysical properties. We show that the probes permit intracellular calcium levels to be assessed by fluorescence, photoacoustic, and magnetic resonance imaging modalities and that they are detectable by multimodal imaging in brain tissue. This work thus establishes a route for monitoring signaling processes over a range of spatial and temporal scales.

Fluorescence

MRI

Ca

Texaphyrin-based calcium sensor

Photoacoustic

KEYWORDS: calcium, cellular signaling, molecular imaging, sensor, texaphyrin

he dynamics of calcium ion concentrations help control a wide array of biological functions, in which calcium ions act as intracellular secondary messengers and participants in cellular excitability. Fluorescent small molecule calcium indicators derived from the calcium chelator 1,2-bis(oaminophenoxy)ethane- $N_1N_2N_1N_3N_3N_4$ -tetraacetic acid (BAPTA)² have been widely applied to study important calcium signaling phenomena, but their utility has mostly been limited to cellular and small animal studies where optical access to regions of interest is feasible. To monitor calcium signaling in deep tissues, less invasive reporting methods are required, such as those employing magnetic resonance imaging (MRI) or photoacoustic tomography (PAT). MRI-compatible calcium probes in particular offer the potential for completely noninvasive imaging of calcium dynamics over large structures such as the brain.³ While in vivo demonstrations of calciumdependent MRI have been reported recently, there remains a need to improve the robustness of noninvasive calcium sensing.

A key challenge in advancing and utilizing MRI technology for calcium imaging is to relate the signals obtained from tissue-level measurements to "ground truth" measurements made at the cellular or near-cellular scale. Although in principle this correlation can be made by combining different probes and imaging methods that each operate at a given level, greater precision, convenience, and reliability are expected for multimodal imaging agents that provide readouts over a range of spatiotemporal scales. In principle, such agents would enable wide-field imaging results to be interpreted in cellular terms. Multimodal agents might also simplify signaling

research by allowing a variety of experimental situations to be investigated using a single probe.

Here, we demonstrate a previously unexplored architecture for multimodal calcium sensors that meets this challenge. It relies on the use of texaphyrins, a class of expanded porphyrin ligands⁶ that can be readily complexed with lanthanide ions.⁷ The hydrolytic stability, ⁸ MRI properties, ⁹ cell permeability, ¹⁰ and biocompatibility of Gd(III)-texaphyrin (MGd) complexes have been demonstrated previously. These complexes are known to produce high contrast in longitudinal relaxation time (T_1) -weighted proton MRI due to the strong dipolar interactions they enjoy with transiently coordinated water molecules.⁹ These interactions benefit specifically from the number of water exchange sites available in MGd (q > 2) and the high spin number afforded by gadolinium (S = 7/2); water relaxation efficiency is proportional to S(S + 1).

The polypyrrolic aromatic core of texaphyrin lanthanide complexes also confers photophysical properties useful for optical imaging, 11 such as strong light absorption bands in the visible range (470–740 nm) and modest fluorescent emission. The combination of relatively low fluorescent quantum yield ($\Phi_{\rm F}=0.0028$ for MGd) and strong absorption also makes Gdtexaphyrin complexes good candidates for PAT. 12 This is because the PAT signal arises from nonradiative relaxation

Received: July 7, 2023 Accepted: September 25, 2023 Published: October 9, 2023





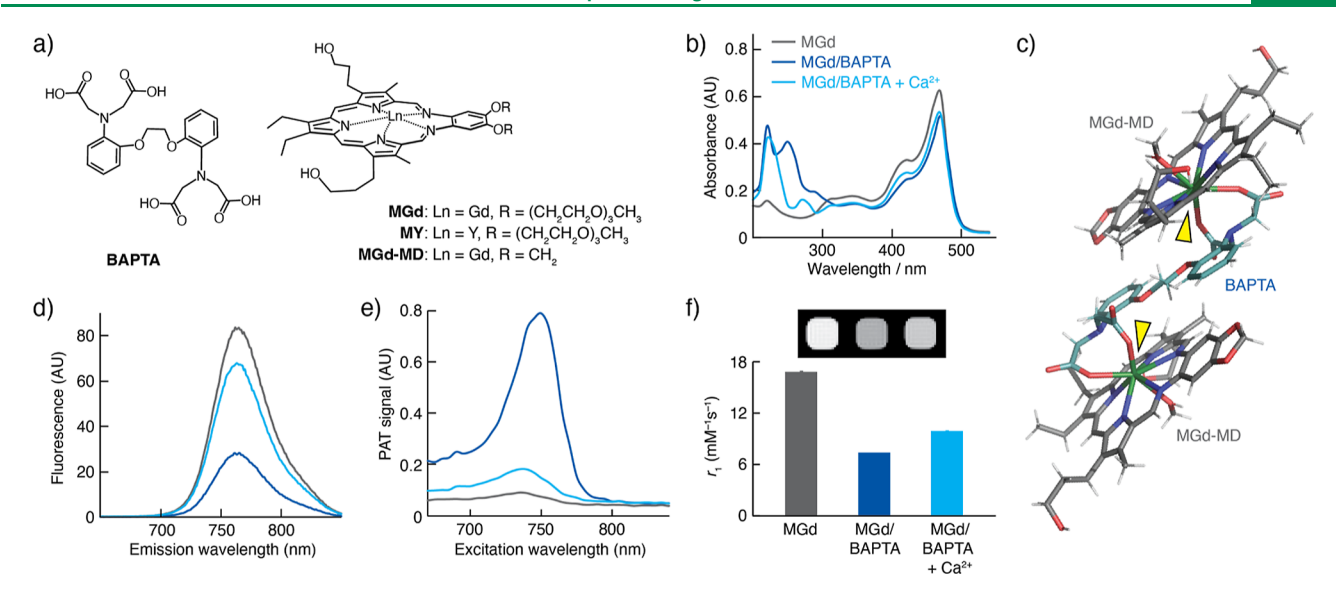


Figure 1. Characterization of a bimolecular texaphyrin-BAPTA model system. (a) Structures of BAPTA (left) and metallotexaphyrin complexes (right) used in this study. (b) UV—vis spectra from 10 μM MGd alone (gray) and in the presence of 30 μM BAPTA, without (blue) or with (cyan) further addition of 70 μM $\rm Ca^{2^+}$. (c) X-ray crystal structure of the complex formed between BAPTA (blue) and the MGd variant MGd-MD (gray). Yellow arrowheads denote sites of interaction between the BAPTA carboxylates and Gd atoms of the two texaphyrin complexes. (d) Fluorescence emission spectra ($\lambda_{\rm ex}$ = 470 nm) corresponding to the UV—vis data in (b). (e) PAT signal as a function of the excitation wavelength. (f) MRI data showing the relaxivity of MGd mixtures (bottom) and corresponding T_1 -weighted images (top). Error bars = standard deviation for n = 3.

from the excited electronic state induced by light absorption, as opposed to fluorescence, which arises from radiative decay. Nonradiative energy deposition generates highly localized heating and pressure changes that can be detected in deep tissue by using ultrasonic readouts. Given these properties, we envisioned that combining BAPTA with an MGd core could generate a trimodal intracellular calcium sensor with complementary functionalities: MRI for whole-brain imaging, PAT for deep tissue mapping with alternative molecular contrast, and fluorescence for the cellular-level validation of probe characteristics.

EXPERIMENTAL SECTION

Full experimental procedures, characterization data, and additional experimental materials are available in the Supporting Information. Descriptions of some of the most important procedures are presented below.

Fluorescence Microscopy. Fluorescence microscopy was carried out on an Olympus IX71 microscope equipped with a Thorlabs camera (C5505MU). The excitation filter was 472/30 nm, and the emission filter was 750/40 nm. HEK293 cells (ATCC) were seeded in glass-bottom 35 mm Petri dishes (MatTrek) at 8×10^5 cells/mL/dish, incubated at 37 °C under 5% CO $_2$ for 24 h. Calcium-sensitive dye (20 μ M) was added, and cells were placed back in the incubator for two more hours. The medium was removed, and the cells were washed three times with phosphate-buffered saline buffer. DAPI (1 μ g/mL) was added to the dish, and cells were incubated for 20 more minutes before being imaged. Images were processed by using the Image] software package.

Photoacoustic Imaging. Photoacoustic data were recorded in the MIT Koch Institute Animal Imaging and Preclinical Testing Core, using a Fujifilm-Visualsonics Vevo3100/LAZRX ultrasound and photoacoustic imaging system equipped with a MX250S transducer (15–30 MHz, center transmit: 21 MHz; axial resolution: 75 μ m). The solutions or cell slurries were injected into polyurethane tubes, which were immobilized by immersion in 1% agarose gel within the sample holder chamber. A layer of ultrasound gel was placed between the agarose gel surface and the transducer. For imaging of ex vivo rat brains, specimens were placed on an agarose gel bed and embedded in ultrasound gel. The transducer was then placed on the superior part of

the brain, and the PAT signal was recorded. For 3D imaging, the interplanar step was set to 152 μ m. The excitation laser wavelength was set at 750 nm.

Magnetic Resonance Imaging. MRI data were acquired on a 7 T AVANCE III Bruker scanner. For in vitro measurements, samples were loaded into wells of a 384-well clear polystyrene plate, which was cut in half to optimally fit the coil. Unused wells were filled with water. Longitudinal (r_1) and transverse (r_2) relaxivity measurements were acquired using a multispin multiecho (MSME) sequence with repetition time (TR) values of 100, 200, 300, 400, 600, 800, 1000, 2000, and 5000 ms with an echo time (TE) of 12 ms or TE values of 12-360 ms with a TR of 5000 ms. Longitudinal (R_1) and transverse (R_2) relaxation rate maps and values were computed from the data using MATLAB. Images presented in the figures depict MRI intensity with or without linear contrast adjustment (grayscale) or R_1 maps (color scale). Relaxivity values reported in the text were computed as the slope of R_1 or R_2 versus probe concentration while calcium titration data were analyzed to obtain EC50 values using a depleting model. Statistical comparisons between paired conditions were performed using the Student's t-test, and all error bars denote the standard deviation from three or more replicate measurements unless otherwise stated.

Intracellular Calcium Measurements. For functional photoacoustic and MRI-based calcium imaging in cells, HEK293F cells (FreeStyle 293-F, Thermo Fisher) were cultured in FreeStyle 293 expression medium at 37 °C under 8% CO₂ before being treated with the contrast agents (50 μ M, 10 \times 10⁶ cells per mL) for 2 h at 37 °C. After being centrifuged at 500g for 5 min, the resulting pellets were washed with calcium-free HBSS buffer. The pellets were centrifuged again and washed two more times. Cells were resuspended in the same buffer to which calcium (various concentrations) and calcimycin (10 μ M) were added. Cells were incubated for 20 min at 37 °C and then centrifuged at 500g for 5 min. The pellets obtained in this way were resuspended in 50 μL of HBSS buffer and either transferred to 384-well plates for relaxivity measurements or placed in tubes (polyurethane) for photoacoustic experiments. Plates were centrifuged for 2 min at 500g and imaged. MRI and photoacoustic data were obtained as described above. Stimulus-dependent R₁ changes in the cells were calculated as $\Delta\Delta R_1(\%) = 100[(\Delta R_{1(Ca2+)} - \Delta R_{1(o)})/$ $\Delta R_{1(\emptyset)}$] with $\Delta R_1 = R_{1(\text{cells}+\text{CaST})} - R_{1(\text{cells})}$, where the subscript labels

Scheme 1. Synthesis of CaST and YCaST^a

"Reaction conditions: (i) triphenylphosphine/diisopropylazodicarboxylate/phthalimide in dichloromethane; (ii) methylamine in methanol; (iii) addition of compound 10 (above), activated with hexafluorophosphate azabenzotriazole tetramethyl uronium (HATU)/diisopropylethylamine in dimethylformamide. Esterase-mediated hydrolysis of the AM groups yields CaST from CaST-AM or YCaST from YCaST-AM.

 Ca^{2+} and ϕ denote the presence and absence of calcium ions, respectively.

For functional fluorescence calcium imaging in cells, FreeStyle 293-F cells (HEK293F, Thermo Fisher) were cultured in FreeStyle 293 expression medium at 37 °C under 8% CO₂ before being treated with YCaST-AM (20 μ M, 10 × 10⁶ cells per mL) for 2 h at 37 °C. Centrifugation at 500g for 5 min gave pellets that were washed with HBSS buffer deprived of calcium. The pellets were centrifuged again and washed two more times. The cells were then resuspended in the same buffer (typically 20 × 10⁶ cells in 2 mL), to which 1 mM calcium and 10 μ M calcimycin were added. Cells were incubated at 37 °C and the fluorescence of the cells in suspension was monitored over time ($\lambda_{\rm ex}$ = 470 nm). The cells were pipetted up and down immediately before each measurement. Equivalent experiments were also performed using the commercially available fluorescent calcium probe Magnesium Green AM (Thermo Fisher), applied at a concentration of 10 μ M, in place of YCaST-AM.

■ RESULTS AND DISCUSSION

To evaluate the feasibility of forming texaphyrin-based calcium sensors, we first studied the interactions between MGd and BAPTA (Figure 1a). Mixing BAPTA as a 30 μ M solution in 3-(N-morpholino)propanesulfonic acid buffer, pH 7.4, with a 10 μM solution of MGd leads to a decrease in the intensity of the two main MGd-derived absorption bands at 470 and 740 nm in the UV-vis spectrum (Figure 1b). This spectral evolution plateaus after about 5 equiv of BAPTA are added. A slight bathochromic shift (2 nm) of the two main maxima is also observed. Such spectral changes have been previously reported for metallotexaphyrins and are thought to arise from axial coordination by new ligands. 13 Two absorption bands at 220 and 250 nm ascribed to BAPTA are seen in the spectrum of the mixture. The lower energy band is suppressed upon the addition of CaCl₂. Corresponding spectral changes are also observed when Ca2+ is added to free BAPTA (Figure S1), so these changes likely reflect interactions between Ca2+ and BAPTA. Long-term stability of MGd itself in the presence of BAPTA was verified by UV-vis spectroscopy and mass spectrometry (Figure S2).

Brown single crystals suitable for X-ray diffraction studies were obtained from a 1:1 mixture of BAPTA and a Gdtexaphyrin variant, MGd-MD (Scheme 1). Structural analysis of these crystals revealed that two metallotexaphyrins bind to

each BAPTA molecule in a sandwich-like arrangement (Figure 1c). ¹⁴ The two quasi-coplanar BAPTA phenyl rings are separated from two of the texaphyrin pyrrole subunits by 3.2 Å. This distance is commensurate with a π - π stacked donor–acceptor interaction that might play a role in stabilizing the overall self-assembled architecture. In the presence of CaCl₂, which is expected to bind to the BAPTA ligand, green single crystals were obtained. In this case, structural analysis revealed that BAPTA was excluded from the crystal lattice. Unit cells contain MGd-MD dimers in which texaphyrin subunits interact through the OH groups of the hydroxypropyl side chains (Figure S3). ¹⁴ These studies thus suggest a structural basis for the spectral changes observed upon mixing MGd, BAPTA, and Ca²⁺.

To determine whether signal changes useful for molecular imaging could be obtained from a combination of MGd and BAPTA, we studied mixtures of these two components using optical spectroscopy, PAT, and MRI. All three modalities revealed signal changes upon putative complex formation and calcium addition. An inverse relationship between fluorescence and PAT signals was observed (Figure 1d,e), as expected from the radiative vs nonradiative relaxation pathways, respectively, associated with the two modalities. Whereas MGd fluorescence emission spectra with excitation at 470 nm were partially quenched (60%) following addition of BAPTA, the PAT signal produced by excitation wavelengths from 680 to 830 nm is increased by about 10-fold. Calcium addition to the MGd/ BAPTA mixture causes a decrease in the PAT signal, while the fluorescence emission recovers to about 80% of the original MGd signal. Analogous T_1 -weighted magnetic resonance measurements (Figure 1f) performed with MGd at 7 T and room temperature reveal reversible changes in longitudinal relaxivity $(r_1$, defined as the slope of $1/T_1$ vs concentration). Addition of BAPTA causes a decrease in the effective r_1 of MGd by up to 58%; this change is partially reversed upon the stoichiometric addition of Ca²⁺.

The promising bimolecular model compound results prompted us to undertake the synthesis of covalent MGd-BAPTA conjugates. The principal conjugate targeted for synthesis, which we termed calcium-sensitive texaphyrin (CaST), is shown in Scheme 1. This compound was formed

by coupling the amine-functionalized texaphyrin derivative MGd(NH₂)¹⁵ to the BAPTA derivative 10^{4b} via an amide linkage (Scheme 1 and Supporting Information). CaST was synthesized as an esterified variant, CaST-AM, in which the BAPTA carboxylate groups are protected by acetomethoxy (AM) groups. These esters are expected to promote cell permeability and intracellular cleavage, following an established paradigm.^{2b}

CaST could be obtained from CaST-AM hydrolysis in a cell-free medium either by treatment with porcine liver esterase (Figure S4) or by incubation in lysate extracted from HEK293F cells (Figure S5), followed by purification using reverse-phase high-performance liquid chromatography. The kinetics of AM ester cleavage were evaluated in the cell lysate, revealing that about 50% was fully hydrolyzed and functional after about 1 h at 37 °C (Figures S6 and S7). LC–MS analysis revealed that conversion to the fully deprotected CaST is complete after about 2 h (Figure 2a). The color of the solution changes from light to dark green upon cleavage, a change that can be reversed upon addition of calcium ions (Figure S8).

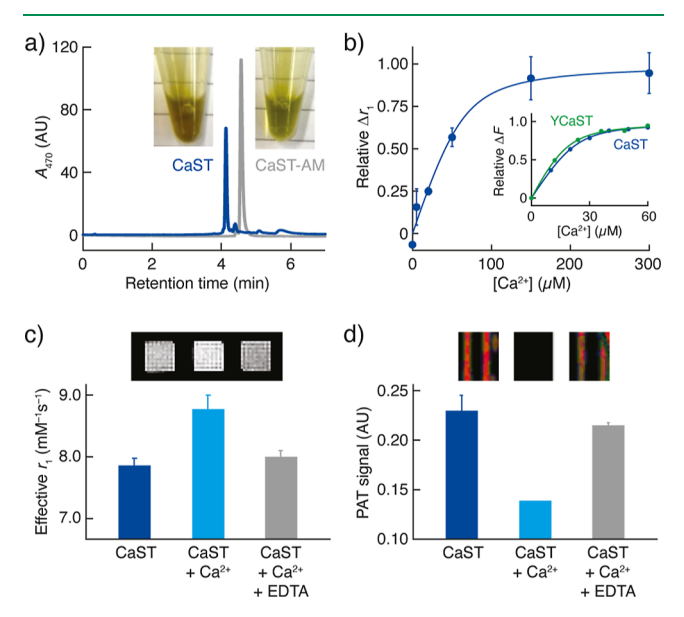


Figure 2. Characterization of CaST-AM in a buffered cell extract. (a) Cleavage of CaST-AM esters after 2 h visualized as a retention time change in reverse-phase LC, with corresponding color change apparent from direct inspection (insets). (b) Relative Δr_1 as a function of calcium concentration, measured by MRI, with analogous fluorescence titration data from CaST (blue) and YCaST (green) shown in the inset. (c) Effective T_1 relaxivity of CaST in cell lysate before and after addition of 300 μ M Ca²⁺, and following further addition of 600 μ M EDTA (bottom). Corresponding images are also shown (top). (d) PAT signal amplitudes from capillary samples analogous to the MRI samples of panel c (bottom). Associated images are shown at the top; red vertical streaks represent photoacoustic emission, which is strongest near the capillary walls. All error bars denote s.d. for n=3.

The calcium binding properties of CaST were further characterized under controlled conditions that emulate the intracellular environment, where the agent was designed to be deployed. Following the incubation of CaST-AM in lysate to promote ester hydrolysis, we performed calcium concentration titrations while monitoring the mixtures using several readout modalities. Titration midpoints (EC₅₀ values) were observed by T_1 -weighted MRI (7 T) and fluorescence ($\lambda_{\rm ex/em} = 470/760$

nm) at 10.5 and 3.2 μ M Ca²⁺, respectively (Figure 2b). These values are suitable for the detection of intracellular [Ca²⁺] fluctuations induced by cell signaling, which fall typically in the 0.1–10 μ M range. Fluorescence spectral titrations were also performed using an yttrium-complexed surrogate, YCaST-AM, which is expected to display a higher quantum yield than gadolinium-based CaST (Φ_F MY = 0.04, 14 times higher than MGd).¹¹ The Ca²⁺ binding EC₅₀ for this yttrium variant was 3.3 μ M, matching the value for the gadolinium-containing probe CaST (Figure 2b, inset) and suggesting that CaST and YCaST are biochemically equivalent.

Responses to calcium addition and subsequent reversal by addition of excess ethylene diamine tetraacetic acid (EDTA) were readily observable by both MRI (Figure 2c) and PAT (Figure 2d) using samples formulated in microtiter plates or in tubes embedded in agarose gel, respectively (Figure S9). The calcium selectivity of these responses was tested by adding magnesium ions instead of Ca2+. In this case, no notable relaxation rate change was observed for CaST (Figure S10). The amplitudes of CaST-dependent signal changes observed upon the addition of 300 μ M Ca²⁺ were 114% in fluorescence (47% for YCaST), 11% in MRI (r_1 change from 7.8 to 8.7 mM⁻¹ s⁻¹), and 40% in PAT. Each of these responses is qualitatively consistent with the calcium-dependent changes observed in the MGd/BAPTA bimolecular mixture in Figure 1. This suggests that interactions between the texaphyrin and calcium-chelating moieties are similar in the noncovalent and covalent complexes.

Critical to the proposed applications of CaST is the need for the AM-protected version of the probe to undergo internalization and ester hydrolysis in intact cells. To assess this, HEK293 cells were incubated with CaST-AM, harvested, and analyzed by inductively coupled plasma mass spectrometry (ICP-MS). The cell pellets obtained after centrifugation were all dark green, as would be expected for samples containing a texaphyrin (Figure S11). Gd quantification revealed that peak uptake was reached after 2 h, with concentrations of 0.22 mM achieved upon incubation with 50 µM CaST-AM. Mass spectrographic analysis confirmed the presence of CaST itself, indicating that full hydrolysis of the CaST-AM esters had occurred (Figure S12). Compared with CaST-AM, roughly 6fold less cell labeling was observed using MGd, which does not undergo AM ester-dependent intracellular trapping. Fractionation analysis of cells incubated with 50 µM CaST-AM indicated that around 20% of the total Gd was localized in soluble fractions (cytosol and nucleosol; Figure S13). Cytotoxicity of CaST-AM was evaluated by an MTT assay. No appreciable evidence of cellular toxicity was seen over 6 h at the concentration used here (Figure S14).

Visualization of cell uptake and calcium responsiveness was carried out by applying CaST-AM or YCaST-AM to HEK293 cells, followed by stimulation with Ca²⁺ in the presence of calcium ionophore calcimycin (Figure 3a). Figure 3b shows microscopy results from cells labeled with 20 μ M YCaST-AM and treated with 10 μ M calcimycin in the presence or absence of 1 mM calcium. A roughly 3-fold enhancement in YCaST fluorescence emission at 750 nm is seen after this stimulation. No appreciable changes are observed in the absence of extracellular Ca²⁺ or in analogous experiments performed with MY, a control yttrium texaphyrin that lacks a BAPTA moiety (Figure 3c). A calcimycin/Ca²⁺-dependent signal increase is also observed following loading of HEK293 cells with 10 μ M of the AM ester form of magnesium green (MgG), a

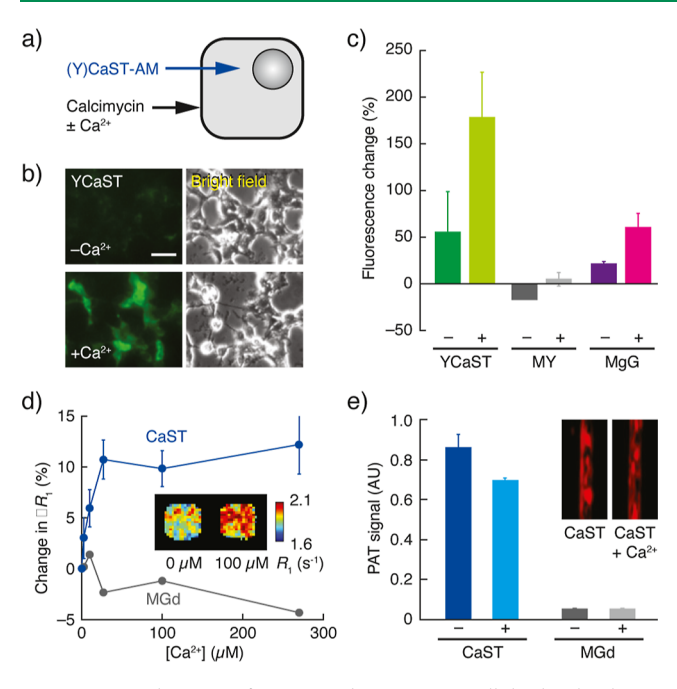


Figure 3. Application of CaST and YCaST to cellular-level calcium imaging. (a) Schematic illustration of cell stimulation with extracellular Ca²⁺/calcimycin after loading with CaST-AM or YCaST-AM. (b) Fluorescence microscopy of HEK293 cells preincubated with 20 μM YCaST-AM and stimulated with 10 μM calcimycin in the absence (top) or presence (bottom) of 1 mM Ca²⁺. Righthand images display corresponding bright field micrographs. Scale bar: 50 µm. (c) Percent change in fluorescence following stimulation in the absence (-) or presence (+) of Ca²⁺ for YCaST, MY, and the commercial fluorescent calcium probe MgG. (d) Percent change in ΔR_1 observed as a function of extracellular calcium concentration in the presence of 10 μ M calcimycin for cells pretreated with CaST-AM (blue) or MGd (gray). The inset shows R_1 maps from representative wells treated with 0 or 100 μ M Ca²⁺. (e) PAT image signal measured from cell slurry samples prepared as for the fluorescence and MRI experiments. The inset shows representative CaST-treated cell slurry images. Error bars denote s.d. for n = 3.

commercial calcium-sensitive fluorophore with a reported calcium dissociation constant of 6 μ M. The relative magnitudes of calcium-dependent signals mediated by MgG and YCaST are similar (Figure 3c).

Analogous experiments were performed with gadoliniumcomplexed CaST-AM, in conjunction with noninvasive imaging readouts. Longitudinal relaxation rate $(R_1 = 1/T_1)$ maps were derived from T_1 -weighted MRI data and revealed calcium-dependent increases in R_1 that are qualitatively similar to results from CaST in cell lysate (Figure 3d, inset). The mean ΔR_1 with respect to unlabeled cells increased by up to 12% over a range of calcium concentrations from 0 to 300 μ M (Figure 3d). The R_1 change amplitude and profile are similar to a recently reported unimodal MRI calcium sensor, 4b with a [Ca²⁺] midpoint of about 10 μ M, close to the EC₅₀ of CaST in cell lysate (Figure 2b). Responses were not observed in cells treated with MGd instead of CaST-AM. Given ICP-MS-based estimates of CaST uptake by these cells, the recorded values of R_1 correspond to an estimated calcium-dependent increase in effective r_1 from 1.60 to 1.85 mM⁻¹ s⁻¹ within the cells.

PAT analysis from CaST-AM-labeled cells shows that the addition of 1 mM Ca²⁺ in the presence of calcimycin induces a 20% decrease in the photoacoustic signal (Figure 3e), paralleling the signal decrease observed in the buffered lysate.

No PAT signal change was observed following cell labeling with MGd, showing that the calcium-dependent response is specific to CaST. As with the MRI measurement, the magnitude of calcium-dependent CaST response observed by PAT is somewhat lower in intact cells than in cell extract, demonstrating consistency between magnetic resonance and photoacoustic modalities.

We next investigated whether CaST-AM could be visualized by multimodal imaging in the rodent brain. Twenty-five μ L of the contrast agent was infused bilaterally into the rat striatum. CaST-AM was injected in the left hemisphere and a 4:1 mixture of CaST-AM and YCaST-AM, expected to show stronger fluorescence signals, was delivered on the right hemisphere; both infusates had the same total concentration of 0.5 mM. Using T_1 -weighted MRI at 9.4 T, we observed substantial brightening on both sides of the brain (Figure 4a,

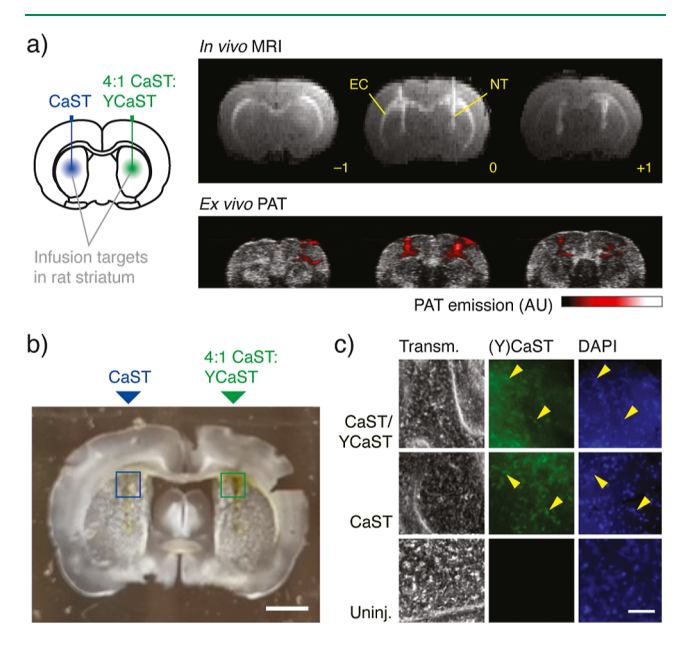


Figure 4. Multimodal imaging of CaST-AM and YCaST-AM in the rodent brain. (a) Wide-field imaging after infusion of CaST-AM or 4:1 CaST-AM:YCaST-AM (schematic at left) into the live rat brain, showing contrast in and around striatal infusion sites in coronal T_1 weighted MRI slices, with enhancement along needle tracks (NT) and external capsule white matter tracts (EC) labeled in yellow, along with bregma coordinates. Corresponding signals in ex vivo PAT scans of the same brain are shown at the bottom. PAT data (color scale) are overlaid on conventional ultrasound images (grayscale). (b) Transmitted light image of a single 50 μ m slice taken from the brain in panel a, indicating injection sites. Scale bar = 2.5 mm. (c) Microscopy images showing transmitted light (left), CaST or YCaST fluorescence (middle), or DAPI fluorescence (right) from the two regions of interest labeled in (b), plus an uninjected striatal region on a different section. Arrowheads indicate representative cells seen in both CaST and DAPI channels. Scale bar = 50 μ m.

top), with contrast enhancement at the striatal target site, up the injection needle tracks, and along nearby white matter tracts. After perfusion and extraction, the brain was imaged ex vivo using PAT, with results showing a strong signal corresponding to the contrast enhancements observed in MRI (Figure 4a, bottom). PAT signal was biased to the more superficial areas of T_1 MRI contrast. This is likely due to the attenuation of laser light in deeper tissue, but a role for calcium

binding in modulating CaST-dependent MRI and PAT contrasts even in these static experiments cannot be ruled out.

The brain in Figure 4a was sliced and mounted on glass in order to examine the optical contrast corresponding to the MRI and PAT images. Slices close to the injection sites showed faint discoloration in the neighborhood of the injection cannula tracts (Figure 4b). Micrographs of select fields of view denoted in Figure 4b reveal 750 nm fluorescence in the neighborhood of CaST-AM injections, with both cellular-scale puncta and background signals indicative of intracellular and extracellular tissue labeling by the probes (Figure 4c). Fluorescence was not notably higher in areas labeled with the 4:1 YCaST/CaST mix, compared with CaST alone, suggesting that the fluorescence signal from the gadoliniumbound probe alone, without a mixture with YCaST, is sufficient for multiscale imaging applications in vivo. In addition to the results in Figure 4, combined in vivo MRI, ex vivo PAT, and cellular-scale fluorescence visualization were performed with two more animals to verify reproducibility (Figure S15).

CONCLUSIONS

Taken in concert, the results presented here validate CaST as a multimodal calcium sensor capable of undergoing cell internalization in its cell-permeant esterase-labile form, CaST-AM. This probe exploits the stable, optically and magnetically active metallotexaphyrin architecture and provides evidence that reversible calcium sensors can be constructed using the MGd platform. Unlike previous singleor dual-modality probes, 4,5 CaST-AM produces MRI, PAT, and fluorescent signal changes dependent on calcium stimulation in labeled cells, constituting a unitary means for cross-validation of signal changes over a range of scales. This work stops short of functional imaging in vivo but shows that multimodal imaging contrast from CaST is visible in complex tissue, thus setting the stage for studies that bridge the gap between cellular physiology and organ- or organism-scale biology in living subjects. Further efforts could also focus on improving the sensitivity of CaST-related calcium probes themselves, for instance, by varying the extent of coupling between the MGd and BAPTA moieties. Extensions of this work could also yield metallotexaphyrin-based multimodal imaging sensors for biologically important analytes in addition to Ca²⁺.

ASSOCIATED CONTENT

Supporting Information

The Supporting Information is available free of charge at https://pubs.acs.org/doi/10.1021/acssensors.3c01387.

Detailed experimental procedures, characterization data, and additional experimental materials (PDF)

Accession Codes

CCDC 2206339 and 2206340 contain the supplementary crystallographic data for this paper. These data can be obtained free of charge via www.ccdc.cam.ac.uk/data_request/cif or by contacting The Cambridge Crystallographic Data Centre, 12 Union Road, Cambridge CB2 1EZ, UK; fax: +44 1223 336033.

AUTHOR INFORMATION

Corresponding Author

Alan Jasanoff — Department of Biological Engineering, Massachusetts Institute of Technology, Cambridge, Massachusetts 02139, United States; oorcid.org/0000-0002-2834-6359; Email: jasanoff@mit.edu

Authors

Grégory D. Thiabaud — Department of Biological Engineering, Massachusetts Institute of Technology, Cambridge, Massachusetts 02139, United States; orcid.org/0000-0001-5189-8445

Miriam Schwalm — Department of Biological Engineering, Massachusetts Institute of Technology, Cambridge, Massachusetts 02139, United States

Sajal Sen – Department of Biological Engineering, Massachusetts Institute of Technology, Cambridge, Massachusetts 02139, United States; orcid.org/0000-0002-1189-4156

Ali Barandov — Department of Biological Engineering, Massachusetts Institute of Technology, Cambridge, Massachusetts 02139, United States

Jacob Simon – Department of Biological Engineering,
 Massachusetts Institute of Technology, Cambridge,
 Massachusetts 02139, United States; Present Address: Jacob Simon, Department of Neurobiology, Stanford University,
 299 W. Campus Drive, (United States)

Peter Harvey — Department of Biological Engineering,
Massachusetts Institute of Technology, Cambridge,
Massachusetts 02139, United States; Present Address: Peter
Harvey, University of Nottingham, Queen's Medical
Centre, NG7 2UH, Nottingham, (U.K.).; orcid.org/
0000-0001-5159-5313

Virginia Spanoudaki – Preclinical Imaging & Testing Facility, Koch Institute at MIT, Cambridge, Massachusetts 02139, United States

Peter Müller – Department of Chemistry, X-ray Diffraction Facility, Cambridge, Massachusetts 02139, United States; orcid.org/0000-0001-6530-3852

Jonathan L. Sessler – Department of Chemistry, The University of Texas at Austin, Austin, Texas 78712-1224, United States; orcid.org/0000-0002-9576-1325

Complete contact information is available at: https://pubs.acs.org/10.1021/acssensors.3c01387

Author Contributions

The manuscript was written through contributions of all authors. All authors have given approval to the final version of the manuscript.

Funding

This work was supported by NIH grants R21 EY032369, U01 NS103470, and R01 NS120592 to A.J., as well as R01 CA68682 to J.L.S. S.S. was supported by a fellowship from the Simons Center for the Social Brain at MIT. J.S. was supported by NIH training grant T32 EB019940, and P.H. was supported by a Wellcome Trust-MIT Postdoctoral Fellowship. Support from the Robert A. Welch Foundation (F-0018) to J.L.S. is also acknowledged.

Notes

The authors declare no competing financial interest.

REFERENCES

- (1) Giorgi, C.; Danese, A.; Missiroli, S.; Patergnani, S.; Pinton, P. Calcium dynamics as a machine for decoding signals. *Trends Cell Biol.* **2018**, 28, 258–273.
- (2) (a) Tsien, R. Y. New calcium indicators and buffers with high selectivity against magnesium and protons: design, synthesis, and

- properties of prototype structures. *Biochemistry* **1980**, *19*, 2396–2404. (b) Tsien, R. Y. A non-disruptive technique for loading calcium buffers and indicators into cells. *Nature* **1981**, 290, 527–528.
- (3) Miller, A. D. C.; Ozbakir, H. F.; Mukherjee, A. Calcium-responsive contrast agents for functional magnetic resonance imaging. *Chem. Phys. Rev.* **2021**, *2* (2), 021301.
- (4) (a) Okada, S.; Bartelle, B. B.; Li, N.; Breton-Provencher, V.; Lee, J. J.; Rodriguez, E.; Melican, J.; Sur, M.; Jasanoff, A. Calcium-dependent molecular fMRI using a magnetic nanosensor. *Nat. Nanotechnol.* 2018, 13, 473–477. (b) Barandov, A.; Bartelle, B. B.; Williamson, C. G.; Loucks, E. S.; Lippard, S. J.; Jasanoff, A. Sensing intracellular calcium ions using a manganese-based MRI contrast agent. *Nat. Commun.* 2019, 10, 897. (c) Savic, T.; Gambino, G.; Bokharaie, V. S.; Noori, H. R.; Logothetis, N. K.; Angelovski, G. Early detection and monitoring of cerebral ischemia using calcium-responsive MRI probes. *Proc. Natl. Acad. Sci. U.S.A.* 2019, 116, 20666–20671.
- (5) (a) Roberts, S.; Seeger, M.; Jiang, Y.; Mishra, A.; Sigmund, F.; Stelzl, A.; Lauri, A.; Symvoulidis, P.; Rolbieski, H.; Preller, M.; Dean-Ben, X. L.; Razansky, D.; Orschmann, T.; Desbordes, S. C.; Vetschera, P.; Bach, T.; Ntziachristos, V.; Westmeyer, G. G. Calcium sensor for photoacoustic imaging. *J. Am. Chem. Soc.* **2018**, *140*, 2718–2721. (b) Adams, C. J.; Krueger, R.; Meade, T. J. A multimodal Ca(II) responsive near IR-MR contrast agent exhibiting high cellular uptake. *ACS Chem. Biol.* **2020**, *15*, 334–341.
- (6) Sessler, J. L.; Johnson, M. R.; Lynch, V. Synthesis and crystal structure of a novel tripyrrane-containing porphyrinogen-like macrocycle. *J. Org. Chem.* **1987**, *52*, 4394–4397.
- (7) (a) Sessler, J. L.; Mody, T. D.; Hemmi, G. W.; Lynch, V. Synthesis and structural characterization of lanthanide(III) texaphyrins. *Inorg. Chem.* **1993**, *32*, 3175–3187. (b) Hannah, S.; Lynch, V.; Guldi, D. M.; Gerasimchuk, N.; MacDonald, C. L. B.; Magda, D.; Sessler, J. L. Late first-row transition-metal complexes of texaphyrin. *J. Am. Chem. Soc.* **2002**, *124*, 8416–8427.
- (8) Sessler, J. L.; Murai, T.; Hemmi, G. W. A water-stable gadolinium(III) complex derived from a new pentadentate "expanded porphyrin" ligand. *Inorg. Chem.* 1989, 28, 3390–3393.
- (9) Sessler, J. L.; Mody, T. D.; Hemmi, G. W.; Lynch, V.; Young, S. W.; Miller, R. A. Gadolinium(III) texaphyrin: a novel MRI contrast agent. *J. Am. Chem. Soc.* 1993, 115, 10368–10369.
- (10) Woodburn, K. W. Intracellular localization of the radiation enhancer motexafin gadolinium using interferometric Fourier fluorescence microscopy. *J. Pharmacol. Exp. Ther.* **2001**, 297, 888–894.
- (11) Guldi, D. M.; Mody, T. D.; Gerasimchuk, N. N.; Magda, D.; Sessler, J. L. Influence of large metal cations on the photophysical properties of texaphyrin, a rigid aromatic chromophore. *J. Am. Chem. Soc.* **2000**, *122*, 8289–8298.
- (12) Ren, Y.; Sedgwick, A. C.; Chen, J.; Thiabaud, G.; Chau, C. V.; An, J.; Arambula, J. F.; He, X. P.; Kim, J. S.; Sessler, J. L.; Liu, C. Manganese(II) texaphyrin: a paramagnetic photoacoustic contrast agent activated by near-IR light. *J. Am. Chem. Soc.* **2020**, *142*, 16156–16160.
- (13) Lammer, A. D.; Thiabaud, G.; Brewster, J. T., II; Alaniz, J.; Bender, J. A.; Sessler, J. L. Lanthanide texaphyrins as photocatalysts. *Inorg. Chem.* **2018**, *57*, 3458–3464.
- (14) Deposition Numbers 2206339 (for [(MGd-MD)₂BAPTA]) and 2206340 (for (MGd-MD)₂) contain the supplementary crystallographic data for this paper. These data are provided free of charge by the joint Cambridge Crystallographic Data Centre and Fachinformationszentrum Karlsruhe Access Structures service.
- (15) Thiabaud, G.; He, G.; Sen, S.; Shelton, K. A.; Baze, W. B.; Segura, L.; Alaniz, J.; Munoz Macias, R.; Lyness, G.; Watts, A. B.; Kim, H. M.; Lee, H.; Cho, M. Y.; Hong, K. S.; Finch, R.; Siddik, Z. H.; Arambula, J. F.; Sessler, J. L. Oxaliplatin Pt(IV) prodrugs conjugated to gadolinium-texaphyrin as potential antitumor agents. *Proc. Natl. Acad. Sci. U.S.A.* 2020, 117, 7021–7029.
- (16) Johnson, I. D.; Spence, M. T. Z. The Molecular Probes Handbook; Life Technologies: Carlsbad, CA, 2010.